Supplementary Materials for

New orbital angular momentum multiplexing strategy: beyond the capacity limit of free-space optical communication

Wenxiang Yan,[1,2] Yuan Gao,[1,2] Xian Long, [1,2] Zheng Yuan,[1,2] Zhi-Cheng Ren,[1,2] Xi-Lin Wang,[1,2] Jianping Ding,[1,2,3,*] and Hui-Tian Wang[1,2,*]

[1]National Laboratory of Solid State Microstructures and School of Physics, Nanjing University, Nanjing 210093, China

[2]Collaborative Innovation Center of Advanced Microstructures, Nanjing University, Nanjing 210093, China

[3]Collaborative Innovation Center of Solid-State Lighting and Energy-Saving Electronics, Nanjing University, Nanjing 210093, China

*Corresponding author: jpding@nju.edu.cn; htwang@nju.edu.cn

Supplementary text:

1. Derivation of equation (3-1): the innermost ring radius of LGB;
2. Self-healing capability of the innermost ring with the aid of sidelobes;
3. Orthogonality, transmission matrix of IRD-OAM multiplexing;
4. Channel crosstalk in IRD-OAM multiplexing;
5. Total reception efficiency $\eta_{total}(m_{max})$ for S^2=6.25 and m_{max} in [0,100];
6. Smallest required quality factors and optimal value of beam waist;

Supplementary Movies: Movies S1-S7.

Supplementary Reference.

Supplementary text

1. Derivation of equation (3-1): the innermost ring radius of LG beam

The amplitude distribution of the LG beam can be written as

$$A_{m,p}(r,\varphi,z)=\left[\frac{w_0}{w(z)}\right]\left[\frac{r}{w(z)}\right]^m \exp(-\frac{r^2}{w^2(z)})L_p^m\left[\frac{2r^2}{w^2(z)}\right]. \tag{S1}$$

Using the approximate relations in refs.[1,2], the right side of Eq. (S1) becomes

$$\left[\frac{r}{w(z)}\right]^m \exp(-\frac{r^2}{w^2(z)})L_p^m\left[\frac{2r^2}{w^2(z)}\right]\approx\frac{\Gamma(p+m+1)}{p!(2N)^{m/2}}J_m(2\sqrt{2N}\frac{r}{w(z)}),p\geq 5,N=p+\frac{m+1}{2}. \tag{S2}$$

The radius of LG beams' innermost ring where the maximum amplitude locates can be derived by searching for the following minimum non-zero solution of $\partial A_{m,p}(r,\varphi,z)/\partial r=0$. Accordingly, it follows that

$$\frac{dJ_m(2\sqrt{2N}\frac{r}{w(z)})}{dr}=0. \tag{S3}$$

Letting $x=2\sqrt{2N}r/w(z)$ and according to equation (5.2.6) in ref.[3] for the Bessel function, $d(J_m(x))/dx=0$ can be rewritten as

$$\frac{dJ_m(x)}{dx}=\frac{1}{2}(J_{m-1}(x)-J_{m+1}(x))=0，\ x>0,m>0. \tag{S4}$$

Although Bessel functions are infinitely extended functions with an infinite number of extreme points, we will focus our attention on the minimum non-zero extreme point, which is located close to the origin. Using the asymptotic formula (5.2.6) in ref. [3],

$$J_m(x)\approx\frac{x^m}{2^m m!}, \tag{S5}$$

for small x that meets our requirement, we obtain the following relation

$$\frac{x^{m-1}}{2^{m-1}(m-1)!}-\frac{x^{m+1}}{2^{m+1}(m+1)!}=0, \tag{S6}$$

and the minimum non-zero extreme point of the mth-order Bessel function expressed by

$$x_m\approx 2\sqrt{m(m+1)}. \tag{S7}$$

Owing to the approximation made in Eqs. (S2) through (S5), the actual position of minimum non-zero extreme point may differ from that determined by Eq. (S7). After scrutinizing the approximating function in Eq. (S7) and the extremum of Bessel function, we figure out a more accurate relation of x_m versus m by introducing into Eq. (S7) two correction constants C_1 and C_2, namely

$$x_m\approx 2C_1\sqrt{m(m+1)}+C_2. \tag{S8}$$

with C_1 and C_2 taking the following values

$$C_1=\begin{cases}0.5207,\ m\leq 40\\ 0.5058,\ m>40\end{cases}\ \text{and}\ C_2=\begin{cases}0.7730,\ m\leq 40\\ 2.0223,\ m>40\end{cases}. \tag{S9}$$

When $m>4$, the error of Eq. (S8) turns out to be less than 1%. For $m\geq 20$, the error is consistently less than 0.5% and remains below 0.1% for larger values of m. Accounting for $x=2\sqrt{2N}r/w(z)$, we obtain the innermost radius of the LG beam at z as below

$$r_m(z)\approx w(z)\frac{C_1\sqrt{(m+1)m}+C_2/2}{\sqrt{2p+m+1}},\quad p\geq 5,m\geq 4 \tag{S10}$$

and Eq. (S11) follows immediately at the beam waist plane (z=0),

$$r_m(0) \approx w_0 \frac{C_1\sqrt{(m+1)m} + C_2/2}{\sqrt{2p+m+1}}, \quad p \geq 5, m \geq 4. \tag{S11}$$

The percent error of Eq. (S11) is shown in Fig. S1. When p<5, the error appears to be large and negative (blue area in Fig. S1), which is ascribed to the approximation in Eq. (S2). When m<4, the error is large and positive (red area in Fig. S1), due to the approximation in Eq. (S5). Noticeably when $p \geq 5$ and $m \geq 4$, the error remains to be below 5% and becomes even smaller and insignificant as p and m increase. For the width of the innermost ring, this error is negligible in most cases. Noteworthily, this error does not change with the propagation position z and the beam waist w_0. Hence the error map of Eq. (S10) is the same as that of Eq. (S11), as shown Fig. S1.

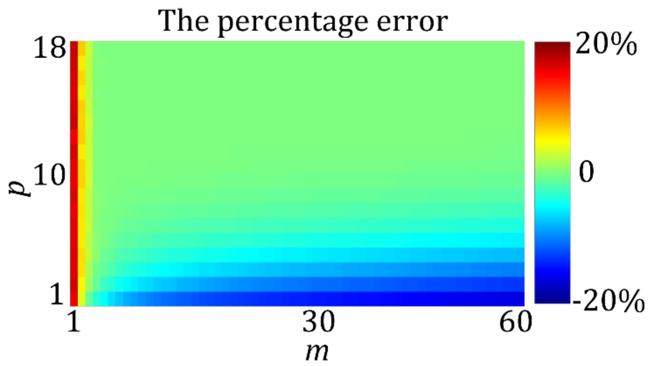

Fig. S1. The percent error of Eq. (S11) varying with *m* and *p*. The percentage error is defined as the ratio between the difference of two innermost radii, respectively calculated from Eq. (S11) and exact LG beams expression, and the exact LGB's innermost radius.

2. Self-healing capability for of the innermost ring with the aid of sidelobes

As illustrated in Fig. S2**a**, a LG beam (m=30, p=12) encounters a square obstacle and gradually reconstructs the impaired innermost ring (the mainlobe) with the aid of sidelobes after propagating through a distance (the experimental setup for generating LG beam and detecting the self-healing progress is the same as ref.[4]). The energy circulation can provide an insightful picture of this self-healing process. The calculated momentum density, as shown in Fig. S2**b**, reveals that despite the azimuthal component of momentum density from the vortex structure is significant, the reconstruction process of the innermost ring is dominated by the radial component, which flows inward from the outer sidelobes. The outer sidelobes can be regarded as a "reservoir" that stores energy for the innermost ring. Without the "energy reservoir" of the sidelobes for p=0, the vortex ring of OAM modes will not self-heal after being impaired, as shown in Figs. S2**c**-**d**.

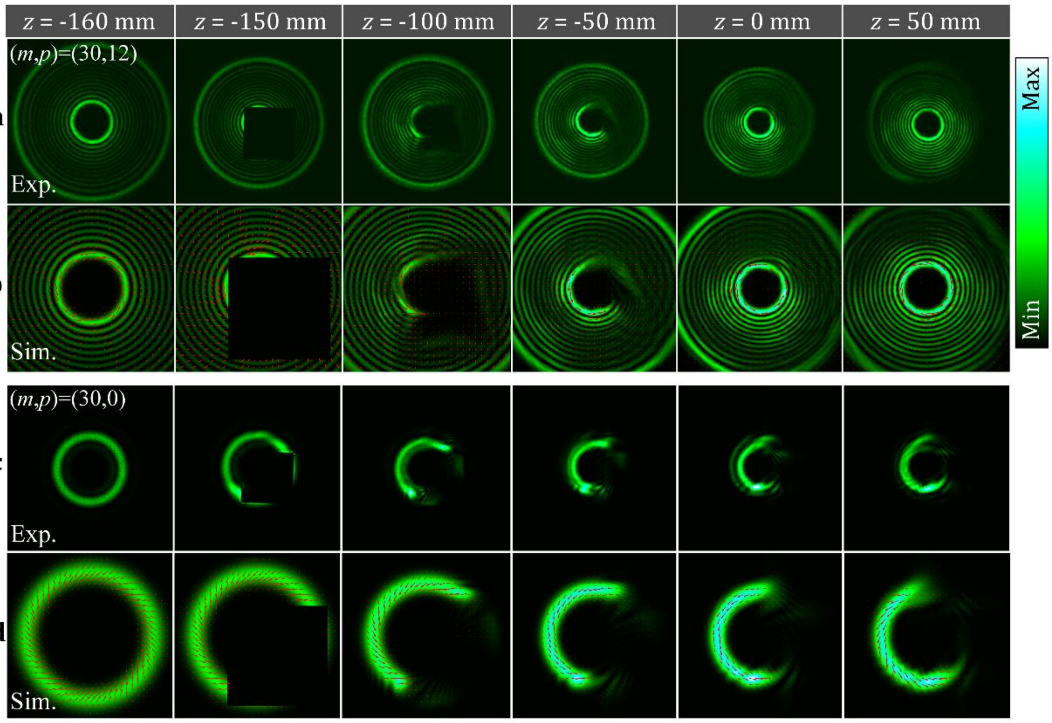

Fig. S2. The self-healing property of the innermost ring of LG beam with nonzero *p*. The LG beam (m = 30, p = 12, w_0 = 0.159 mm, z_0 = 150 mm) is blocked by a square obstacle at z = -150 mm: **a** Experimental intensity maps at different z-axial locations (Supplementary Movie S3); **b** Transversal momentum flow density of **a**, following from the cycle-average Poynting vector given by $\boldsymbol{p} = \varepsilon_0/(2\omega)\mathrm{Im}[\boldsymbol{U}^* \times (\nabla \times \boldsymbol{U})]$ (ε_0, the vacuum permittivity; ω, circular frequency)[5], the red arrows indicate the value and direction of each flow (Supplementary Movie S4); **c**-**d** are the same as **a**-**b** but for p = 0 (Supplementary Movies S5-S6). The sharp-edged square obstacle is produced as masks via the process of photoetching chrome patterns on a glass substrate.

3. Orthogonality, transmission matrix of IRD-OAM multiplexing

The orthonormality of the normalized LG beam in Eq. (1), as illustrated in Fig. S3**a**, can be expressed as

$$\begin{aligned}\left\langle \mathrm{LG}_{m_1,p_1} \middle| \mathrm{LG}_{m_2,p_2} \right\rangle &= \iint_{\infty} \mathrm{LG}_{m_1,p_1}(r,\varphi,z_1) \times \mathrm{LG}^*_{m_2,p_2}(r,\varphi,z_1)\, r dr d\varphi \\ &= \int_0^{\infty} \mathrm{LG}_{m_1,p_1}(r,z_1) \times \mathrm{LG}^*_{m_2,p_2}(r,z_1)\, r dr \int_0^{2\pi} e^{im_1\varphi} e^{-im_2\varphi} d\varphi = \delta_{(m_1,m_2),(p_1,p_2)},\end{aligned} \tag{S12}$$

where $\mathrm{LG}_{m,p}(r,\varphi,z_1) = \mathrm{LG}_{m,p}(r,z_1)e^{im\varphi}$. When the circular receiver aperture circ($r/R_0(z_1)$) truncates the LG beam, with circ($\cdot$) denoting the circular function, Eq. (S12) becomes

$$\begin{aligned}
&\left\langle \mathrm{LG}_{m_1,p_1}\,\mathrm{circ}\left(r/R_0\left(z_1\right)\right)\middle|\mathrm{LG}_{m_2,p_2}\,\mathrm{circ}\left(r/R_0\left(z_1\right)\right)\right\rangle \\
&=\iint_{\infty}\mathrm{LG}_{m_1,p_1}\left(r,\varphi,z_1\right)\times\mathrm{LG}^{*}_{m_2,p_2}\left(r,\varphi,z_1\right)\mathrm{circ}\left(r/R_0\left(z_1\right)\right)rdrd\varphi \\
&=\int_0^{R_0(z_1)}\mathrm{LG}_{m_1,p_1}\left(r,z_1\right)\times\mathrm{LG}^{*}_{m_2,p_2}\left(r,z_1\right)rdr\int_0^{2\pi}e^{im_1\varphi}e^{-im_2\varphi}d\varphi \\
&=\left(\int_0^{\infty}\mathrm{LG}_{m_1,p_1}\left(r,z_1\right)\times\mathrm{LG}^{*}_{m_2,p_2}\left(r,z_1\right)rdr-\int_{R_0(z_1)}^{\infty}\mathrm{LG}_{m_1,p_1}\left(r,z_1\right)\times\mathrm{LG}^{*}_{m_2,p_2}\left(r,z_1\right)rdr\right)\int_0^{2\pi}e^{im_1\varphi}e^{-im_2\varphi}d\varphi \\
&=\delta_{(m_1,m_2),(p_1,p_2)}-2\pi\delta_{(m_1,m_2)}\int_{R_0(z_1)}^{\infty}\mathrm{LG}_{m_1,p_1}\left(r,z_1\right)\times\mathrm{LG}^{*}_{m_2,p_2}\left(r,z_1\right)rdr
\end{aligned}\tag{S13}$$

If $m_1 \neq m_2$, Eq. (S13) equals 0, thus verifying the orthogonality of distinct azimuthal modes (i.e. OAM orthogonality), as shown in Fig. S3**b**. When $m_1=m_2=m$ but $p_1 \neq p_2$, Eq. (S13) can be expressed as

$$\left\langle \mathrm{LG}_{m,p_1}\,\mathrm{circ}\left(r/R_0\left(z_1\right)\right)\middle|\mathrm{LG}_{m,p_2}\,\mathrm{circ}\left(r/R_0\left(z_1\right)\right)\right\rangle=-2\pi\int_{R_0(z_1)}^{\infty}\mathrm{LG}_{m_1,p_1}\left(r,z_1\right)\times\mathrm{LG}^{*}_{m_2,p_2}\left(r,z_1\right)rdr\ ,\tag{S14}$$

which is nonzero for a limited-size aperture. As a result of the the limited-size receiver aperture, distinct radial modes are no longer orthogonal, as shown in Fig. S3**c**. Accordingly, each m can only have one optimal radial index $p_{opt}(m)$ in this mode-division multiplexing, which enables independent and low-crosstalk subchannels in orthogonally OAM demultiplexing. The orthogonality of the truncated normalized LG beam, $\mathrm{LG}_{m,p_{opt}(m)}(r,\varphi,z_1)\mathrm{circ}(r/R_0(z_1))$, can be expressed as

$$\left\langle \mathrm{LG}_{m_1,p_{opt}(m_1)}(r,\varphi,z_1)\mathrm{circ}(r/R_0(z_1))\middle|\mathrm{LG}_{m_2,p_{opt}(m_2)}(r,\varphi,z_1)\mathrm{circ}(r/R_0(z_1))\right\rangle=\begin{cases}0 & m_1\neq m_2\\ \eta(m) & m_1=m_2=m\end{cases},\tag{S15}$$

where the receiving efficiency $\eta(m)$, which is the ratio of power falling in aperture to the entire beam, is represented by $\left\langle \mathrm{LG}_{m,p_{opt}(m)}(r,\varphi,z_1)\mathrm{circ}(r/R_0(z_1))\middle|\mathrm{LG}_{m,p_{opt}(m)}(r,\varphi,z_1)\mathrm{circ}(r/R_0(z_1))\right\rangle$. From Eq. (S15), we can rebuild the orthonormalized relation for the truncated LG beams as follows

$$\left\langle \frac{\mathrm{LG}_{m_1,p_{opt}(m_1)}(r,\varphi,z_1)\mathrm{circ}(r/R_0(z_1))}{\sqrt{\eta(m_1)}}\middle|\frac{\mathrm{LG}_{m_2,p_{opt}(m_2)}(r,\varphi,z_1)\mathrm{circ}(r/R_0(z_1))}{\sqrt{\eta(m_2)}}\right\rangle=\delta_{m_1,m_2}.\tag{S16}$$

The orthonormality of Eq. (S16) is illustrated in Fig. S3**d**.

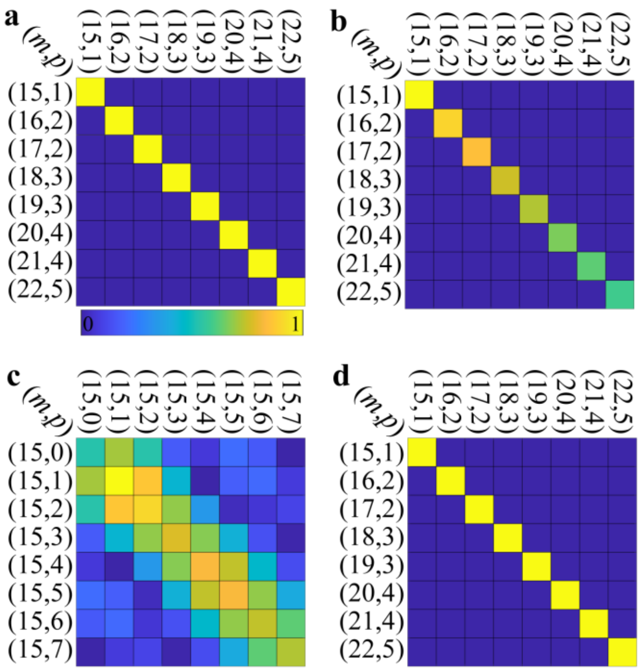

Fig. S3. Orthogonality of truncated LG beams with *m*. a Confusion matrix of normalized LG beams with modes identical to Fig. 1**e**. **b** Confusion matrix of truncated LG beams with distinct *m*, which are truncated by the receiver aperture (the yellow-dotted circles) in Fig. 1**e**. **c** Confusion matrix of truncated LG beams with the same *m*=15 and distinct *p*. **d** Confusion matrix of the orthonormalized truncated LG beams in Eq. (S16).

Let the transmitted and received signals at time t be $\boldsymbol{s}(t)=\begin{bmatrix} s_1(t) & s_2(t) & \cdots & s_M(t)\end{bmatrix}$ and $\boldsymbol{r}(t)=\begin{bmatrix} r_1(t) & r_2(t) & \cdots & r_M(t)\end{bmatrix}$. As the FSO system is linear, the input and output are related by a transmission matrix $\boldsymbol{h}$ so that $\boldsymbol{r}(t)=\boldsymbol{h}\cdot\boldsymbol{s}(t)$. Under the assumption of perfect OAM demultiplexing, the transmission matrix of IRD-OAM multiplexing is diagonal. The matrix elements is represented by $h_{l,n}=\sqrt{\eta_{\max}(m)}\delta_{l,n}$ for the information carrier, $\sum_{-m_{\max}}^{m_{\max}} A_m(t)e^{i\phi_m(t)}\mathrm{LG}_{m,p_{opt}(m)}(r,\varphi,z)$, that has the equal transmitting power in each subchannel, and by $h_{l,n}=\delta_{l,n}$ for the normalized information carrier, $\sum_{-m_{\max}}^{m_{\max}} A_m(t)e^{i\phi_m(t)}\mathrm{LG}_{m,p_{opt}(m)}(r,\varphi,z)/\sqrt{\eta_{\max}(m)}$, that has the equal receiving power in each subchannel[6]. Since the off-diagonal elements of $\boldsymbol{h}$ are zeros, the IRD-OAM multiplexing promises minimal channel crosstalk in communication experiments.

4. Channel crosstalk in the IRD-OAM multiplexing

To evaluate the inter-channel crosstalk in the IRD-OAM multiplexing quantitatively, we simulated the power leakage among channels and calculated crosstalk for each channel, as shown in Fig. S4. As an example of 8-bit IRD-OAM multiplexing, the crosstalk for a channel 1 (Bit 1) can be calculated by the following formula: 10lg[P_{Bit1}(coding:01111111) / P_{Bit1} (coding:10000000)], where the numerator and denominators in the ratio represent the power accumulated within the region of Bit 1 when transmitting the codes of “01111111” and “10000000”, respectively. To maintain consistency, the size of the accumulated region size is fixed at 32 pixels.

Figure S4**a** shows that the channel crosstalk of 8-bit IRD-OAM multiplexing (Fig. 4) is around −20 dB for Δm=2; Figure S4**b** shows that the channel crosstalk of 24-bit IRD-OAM multiplexing (Fig. 5) is below −20 dB for Δm=2 and 4; Figure S4**c** shows a channel crosstalk of −16 dB in the 77-bit IRD-OAM multiplexing with m ranging from -38 to 38 for Δm = 1 and SNR=(N_0-6.38) dB. The channel crosstalk of IRD-OAM multiplexing (the red and green curves for $\sum_{-m_{\max}}^{m_{\max}} A_m(t)e^{i\phi_m(t)}\mathrm{LG}_{m,p_{opt}(m)}(r,\varphi,z)/\sqrt{\eta_{\max}(m)}$ and $\sum_{-m_{\max}}^{m_{\max}} A_m(t)e^{i\phi_m(t)}\mathrm{LG}_{m,p_{opt}(m)}(r,\varphi,z)$ respectively) and traditional OAM multiplexing without a receiving aperture (the blue curves) are at the same level. Besides, Figure S4**c** shows that the channel crosstalk of 181-bit IRD-OAM multiplexing with m=-80, -79, ..., 79, 80 (Δm = 1) and SNR=(N_0 -10) dB is around -13dB (the red curve), and increasing the modal interval to Δm = 2 with m = -80, -78, ..., 78, 80 (the red-dotted curve) can sharply lower the crosstalk, as in conventional OAM multiplexing. The low channel crosstalk ensures the high accuracy and robustness of IRD-OAM multiplexing in the FSO system.

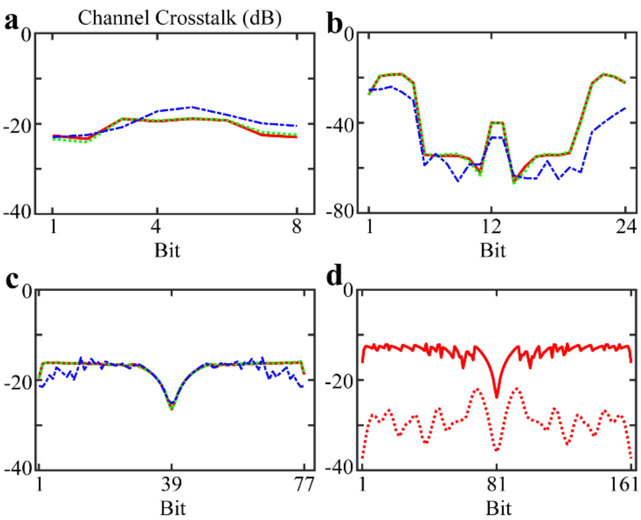

Fig. S4. Channel crosstalk in demultiplexing of **a** 8-bit IRD-OAM multiplexing in Fig. 4 of the main text, **b** 24-bit IRD-OAM multiplexing in Fig. 5, **c** 77-bit IRD-OAM multiplexing with m_{max} = 38 and SNR = (N_0-6.38) dB, **d** 161-bit IRD-OAM multiplexing with m_{max} = 80 and SNR = (N_0-10) dB. The red, green, and blue curves in **a-c** depict the channel crosstalk of $\mathrm{LG}_{m,p_{opt}(m)}(r,\varphi,z_1)\mathrm{circ}(r/R_0(z_1))/\sqrt{\eta(m)}$, $\mathrm{LG}_{m,p_{opt}(m)}(r,\varphi,z_1)\mathrm{circ}(r/R_0(z_1))$, and $\mathrm{LG}_{m,p_{opt}(m)}(r,\varphi,z_1)$, respectively. The red and red-dotted curves in **d** represent the channel crosstalk of IRD-OAM multiplexing with m = -80, -79, ..., 79, 80 (Δm=1) and with m = -80, -78, ..., 78, 80 (Δm=2).

The simulated results displayed in Fig. S4 confirm the low crosstalk between the information carriers, $\sum_{-m_{\max}}^{m_{\max}} A_m(t)e^{i\phi_m(t)}\mathrm{LG}_{m,p_{opt}(m)}(r,\varphi,z)/\sqrt{\eta_{max}(m)}$ and $\sum_{-m_{\max}}^{m_{\max}} A_m(t)e^{i\phi_m(t)}\mathrm{LG}_{m,p_{opt}(m)}(r,\varphi,z)$ (denoted by IC1 and IC2 hereinafter, respectively), in the IRD-OAM multiplexing. It should be noted, however, that IC1 has lower channel crosstalk than IC2 due to variations in the receiving power of each subchannel in IC2 from $\eta_{max}(1)$=1 to $\eta_{max}(m_{max})$ (Equation S15), resulting in an increase in crosstalk during demultiplexing. In contrast, IC1 has equal receiving power for each subchannel (Equation S16). For example, when m_{max} = 38, the SNRs of each channels for IC1 is uniform (N_0-ΔN(m))= (N_0-6.38) dB while those for IC2 vary from N_0 to (N_0-10) dB. This brings greater crosstalk in demultiplexing, particularly when the number of multiplexing channels is large. As a validation, we replaced IC1 with IC2 for the 8-bit IRD-OAM multiplexing experiment in Fig. 4**b-d**. We observed that due to the higher modal crosstalk, IC2 had a smaller discrimination threshold range with [0.15, 0.25] for a zero bit error rate. Therefore, we have chosen IC1 for IRD-OAM multiplexing in this study.

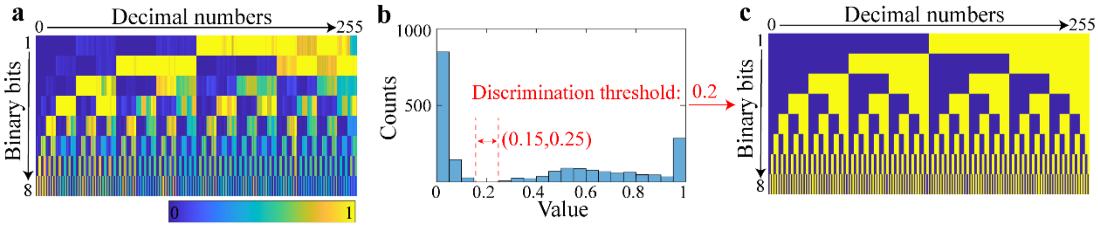

Fig. S5. Experimental demonstration for IC2 in 8-bit IRD-OAM multiplexing. a-c Same as Fig.4 **b-d** but based on IC2 with discrimination threshold 0.2. Supplementary Movie S7 shows the experimental demultiplexing intensity maps of the 256 cases on the camera.

5. Total reception efficiency $\eta_{total}(m_{max})$ for S^2=6.25 and m_{max} in [0,100]

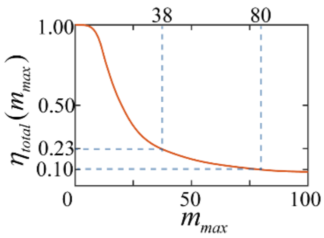

Fig. S6. Total reception efficiency $\eta_{total}(m_{max})$ with S^2=6.25 for m_{max} in [0,100]. The blue-dashed lines show $\eta_{total}(38)$=0.23, $\eta_{total}(80)$= 0.10.

6. Smallest required quality factors and optimal value of beam waist

For the FSO communication with the desired capacity of Q=21, the minimum required quality factors of the FSO systems for the OAM multiplexing and the LG beam multiplexing are S^2 =10 (by solving $2S^2+1=21$) and S^2 =6 (by solving $0.5S^2(S^2+1)=21$). For the IRD-OAM multiplexing with $Q_{IRD\text{-}OAM}= 2m_{max}+1=21$ and thus m_{max}=10. When the receiver aperture is reduced to $R_0=0.85W(z_1)$ with $S^2=0.85^2=0.72$, the SNR is N_0−10 dB ($\eta_{total}(m_{max}=10)=0.1$), shown in Fig. S7

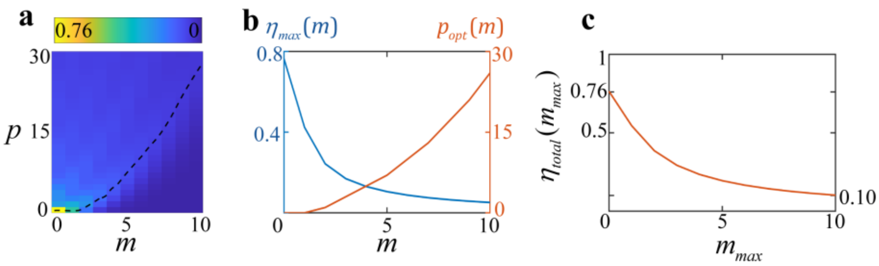

Fig. S7. Receiving efficiency of LG beams with the receiver aperture of $R_0=0.85W(z_1)$ and S^2=0.72. **a** Receiving efficiency with m equals 0, 1, ..., 10 and p equals 0, 1, ..., 30 respectively; the dashed line represents the maximum efficiency $\eta_{max}(m)$ and corresponding radial orders $p_{opt}(m)$, shown in **b**. **c** the total receiving efficiencies $\eta_{total}(m_{max})$, depicting that $\eta_{total}(10)$=0.10.

Since the beam waist w_0 is unrelated to the beam/system quality factors which are primarily examined in the paper, the value of w_0 has no bearing on the improvement in Fig. 6. However, for a fixed link distance z_1, by solving $w(z_1)=\sqrt{w_0^2+\frac{{z_1}^2\lambda^2}{\pi^2 w_0^2}}$ with respect to w_0, there does exist an optimal $w_0=\sqrt{z_1\lambda/\pi}$ to achieve the smallest beam/innermost ring/aperture size with $\mathrm{Min}(w(z_1))=\sqrt{2z_1\lambda/\pi}=\sqrt{2}w_0$. For example, like z_1=2.49 m in Fig. 4**a**, in contrast to the experimental values of w_0=374 μm and $w(z_1$=2.49 m)=1200 μm, the optimal value of w_0 is 648 μm and corresponding Min($w(z_1$=2.49 m))= 916 μm but the corresponding LG beams with the optimal value of w_0 are too large to be generated by our SLM1.

Supplementary Movies

Movie S1. Those 77 subchannels of IRD-OAM multiplexing for m_{max}=38 in the FSO link system S^2=6.25.

Movie S2. Experimental demultiplexing intensity maps of the 256 cases on the Camera of Figs. 4**b**-**d**.

Movie S3. Experimental movie for the self-healing process of LGB's innermost ring (m = 30, p = 12) with the aid of sidelobes in Fig. S2**a**.

Movie S4. Corresponding transversal energy flow density of the self-healing process in Fig. S2**b**.

Movie S5. Experimental movie that the innermost ring will not self-heal after impaired without the "energy reservoir" of the sideloes when p=0, shown in Fig. S2**c**.

Movie S6. Corresponding transversal energy flow density shown in Fig. S2**d**.

Movie S7. Experimental demultiplexing intensity maps of the 256 cases on the camera of Fig. S5.

Reference

1 Mendoza-Hernández, J., Hidalgo-Aguirre, M., Ladino, A. I. & Lopez-Mago, D. Perfect Laguerre–Gauss beams. *Opt. Lett.* **45**, 5197-5200 (2020).

2 Mendoza-Hernandez, J., Arroyo-Carrasco, M. L., Iturbe-Castillo, M. D. & Chavez-Cerda, S. Laguerre-Gauss beams versus Bessel beams showdown: peer comparison. *Opt. Lett.* **40**, 3739-3742 (2015).

3 Silverman, R. A. *Special functions and their applications*. (Courier Corporation, 1972).

4 Yan, W. *et al.* Non-diffracting and self-accelerating Bessel beams with on-demand tailored intensity profiles along arbitrary trajectories. *Opt. Lett.* **46**, 1494-1497 (2021).

5 Bekshaev, A., Bliokh, K. Y. & Soskin, M. Internal flows and energy circulation in light beams. *Journal of Optics* **13**, 053001 (2011).

6 Zhao, N., Li, X., Li, G. & Kahn, J. M. Capacity limits of spatially multiplexed free-space communication. *Nat. photonics* **9**, 822-826 (2015).